1_C51

Three-Dimensional Characterization Of The Air Infiltration Path Using Infrared Technology

Raquel Gil-Valverde **Diego Tamayo-Alonso** **Andrés Royuela-del-Val**

Irene Poza-Casado **Héctor Jimeno-Merino** **Alberto Meiss, PhD**

M. A. Padilla-Marcos, PhD **Jesús Feijó-Muñoz, PhD**

ABSTRACT

Air infiltration control is essential to guarantee thermal comfort, good performance of the ventilation systems, and more energy-efficient buildings. The evaluation of the global airtightness of the building envelope based on pressurization tests has been widely used combined with infrared thermography as a complementary tool to locate air leakage paths. This work proposes a new methodology whose main objective is the characterization of the air infiltration path using infrared thermography.

By means of laboratory experimental measurements, the three-dimensional definition of the air temperature entering a built space through a controlled envelope gap was made. This method is based on the bidimensional temperature matrix of the infiltration path close to the opening depending on different configurations of the air inlet and flows, obtained from infrared images. The image capture was done using a non-continuous representation surface in order to avoid the Coanda effect that continuous surfaces cause, achieving in that way an increase of 42% in the measuring accuracy. This method sets the basis for the quick evaluation by thermal analysis of the air infiltration path produced through air leakages in the building envelope.

INTRODUCTION

IR thermography is a technique that allows the measurement of the temperature of an object without having contact with it (Sarawade 2018). The use of this technology in the construction sector is nowadays more frequent for detecting thermal irregularities, air leakages and moisture abnormalities on building envelopes (Kirimtat and Krejcar 2018) and its relationship with the energy losses (González-Aguilera et al. 2013). Some authors combine the monitorization of the temperatures with the use of IR cameras to observe the evolution of the temperatures in the constructive imperfections all along the day, avoiding in that way the error due to the interpretation of single data to associate every type of error with an IR representation (Fox et al. 2015), (Lehmann et al. 2013). The perception of the same defect from the interior and exterior of the building has been also studied in order to compare both images of the same phenomenon (Fox, Goodhew, and De Wilde 2016).

Specifically, the use of thermography to detect and quantify air infiltration has already been studied (Barreira, Almeida, and Moreira 2017), (Lerma, Barreira, and Almeida 2018) and (Royuela-del-Val et al. 2019). Some authors have

Raquel Gil-Valverde and **Héctor Jiménez-Merino** are research assistants, **Diego Tamayo-Alonso** is an Architect, **Andrés Royuela-del-Val a**nd **Irene Poza-Casado** are predoctoral fellows, **Miguel Ángel Padilla-Marcos** is an Assistant Professor, **Alberto Meiss** is an Associate Professor and **Jesús Feijó-Muñoz** is a Full Professor in the *Department of Construcciones Arquitectónicas, IT y MMC y TE* at the *Escuela Superior de Arquitectura*, Universidad de Valladolid, Spain and members of the RG Arquitectura&Energía.

determined the parameters of a crack measuring the temperatures in the surface of the infiltration plane (Dufour, Derome, and Zmeureanu 2009), (Liu, Zhao, and Chen 2018). Furthermore, thermography has been used combined with neural networks to predict the airflow based on the temperature variation around the air leakage path (Royuela-del-Val et al. 2019).

This research proposes a new technique based on previous studies with a reduction of the Coanda effect, improving in this way, the accuracy of the values obtained. In this way, two main stages can be distinguished. The first one had the objective to demonstrate that a non-continuous surface represents the air path caused by infiltration with more accuracy than a continuous one due to the Coanda effect. Afterwards, based on the results of the previous stage, measurements of the air path at different points were systematized in order to represent it three-dimensionally.

METHODOLOGY

Equipment and laboratory experimental set-up

The test was carried out in a controlled test chamber with a size of 3.0 m x 4.0 m x 2.5 m (height). It had three openings that can be configurated as inlet or outlet (Figure 1).

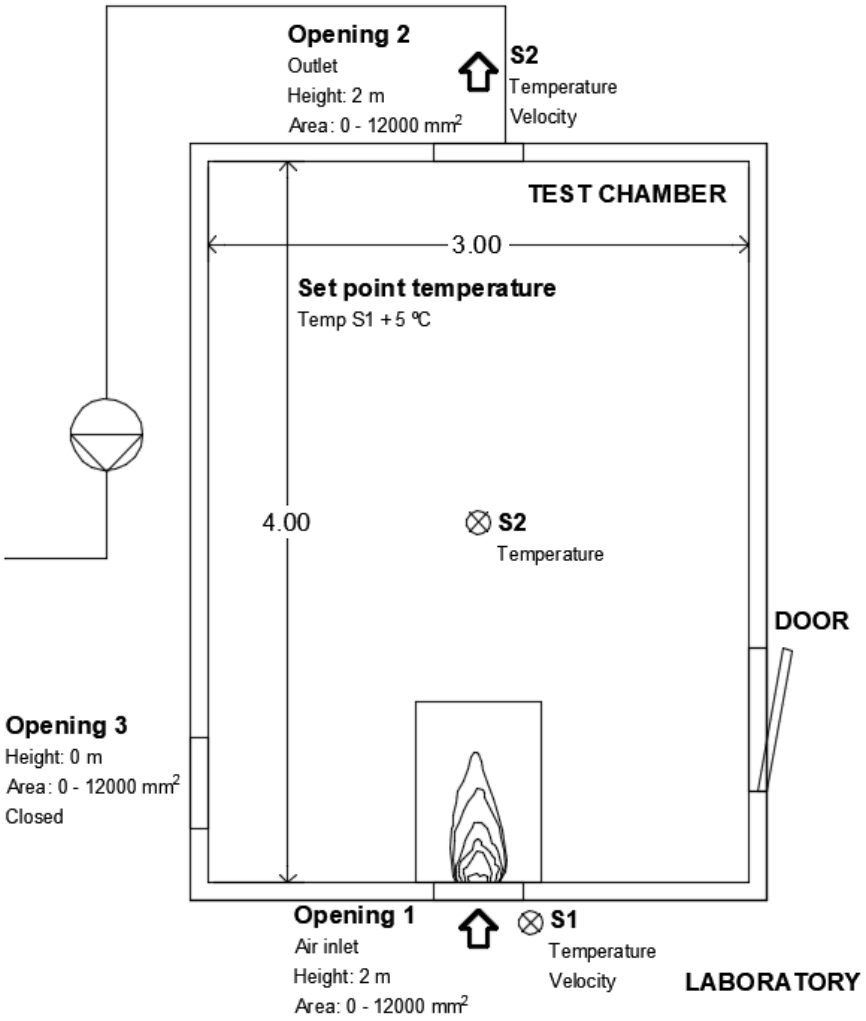

Figure 1. Test chamber configuration floor plan

The test was performed with three different air inlets made by additive 3D printing, which guaranteed the accuracy of the dimensions. The inlets had the same height and different widths, corresponding therefore to three air inlet areas (Figure 2).

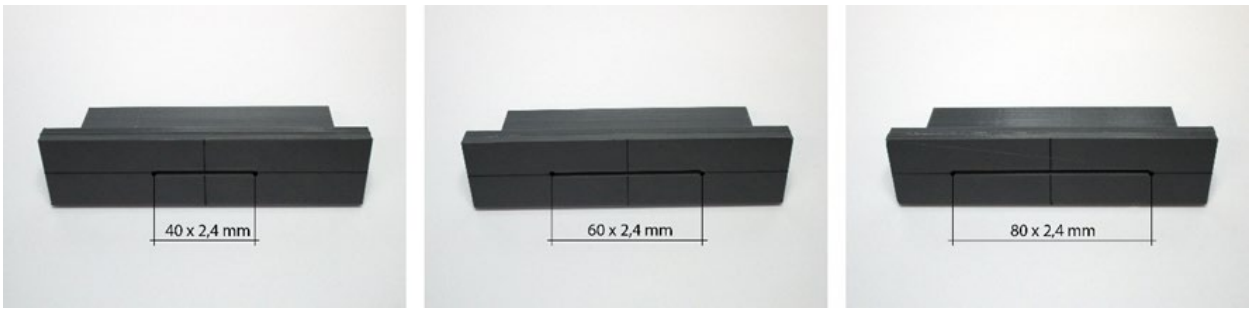

Figure 2. Incoming airflow openings a) A1. 40 mm x 2.4 mm (96 mm^2) b) A2. 60 mm x 2.4 mm (144 mm^2) c) A3. 80 mm x 2.4 mm (192 mm^2)

The monitorization of the airflow through the test chamber and other parameters as inlet and outlet air temperatures was done by a data acquisition system composed of two multisensory data loggers. The temperature was measured with a high precision sensor with an accuracy of ±0.1 K, whereas the airflow was measured with a thermal mass flow sensor with an accuracy of < 3 % of the measured value.

For the thermal images capture, an IR camera with a resolution of 320 x 240 was used. A rendering surface 1.5 mm thick meshed with 10 mm squared cells and made of a material with emissivity ε=0.99 was used to photograph the air path (Figure 3). The size of the grid was empirically obtained: Coanda effect can be considered negligible for grids bigger than 10 mm. Larger grid sizes meant the loss of nodes and, therefore, a reduction of accuracy of the measurement.

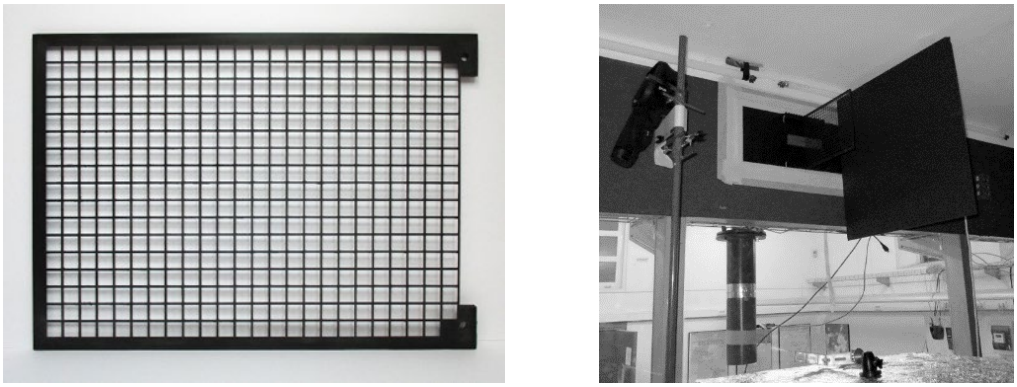

Figure 3. a) Meshed surface 240 mm x 180 mm in black PLA with 10 x 10 mm squared cells. b) Set up for the vertical test.

The configuration of the test chamber was done with the inlet and outlet opposite one another. The airtightness of the chamber guaranteed an equilibrated airflow perpendicular to the wall where the incoming airflow opening was located. In order to create a negative pressure to cause the movement of the air, a fan connected to a frequency variator for its control was used. The electric underfloor radiant system with low thermal inertia of the chamber (Figure 4) was activated to ensure around 5 ºC temperature difference between the interior and the exterior of the test chamber, guaranteeing in this way good reproduction of the infrared images. A Lambert radiator was located under the inlet to avoid the thermal radiation due to the heating system.

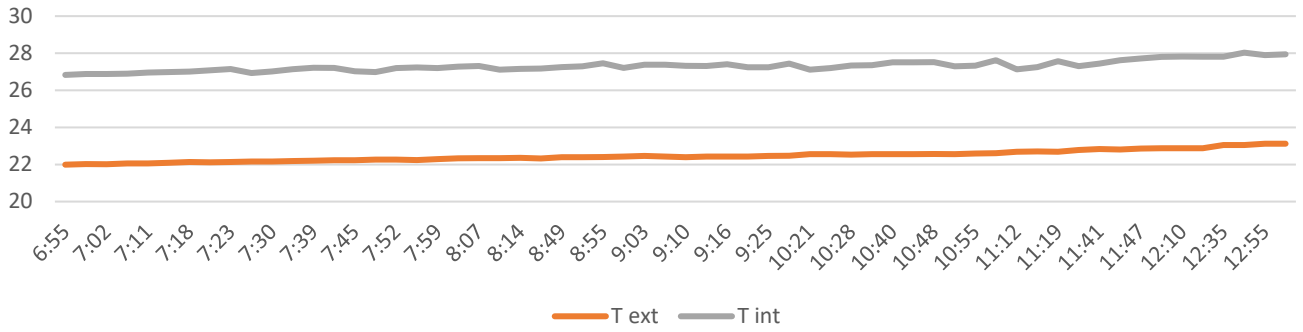

Figure 4. Average data of the temperatures registered during the tests

Experimental design and data processing

During the test, IR thermal images were captured always after the stabilization of the temperatures in different planes: YZ, or vertical plane, and XZ, or horizontal plane (Figure 5).

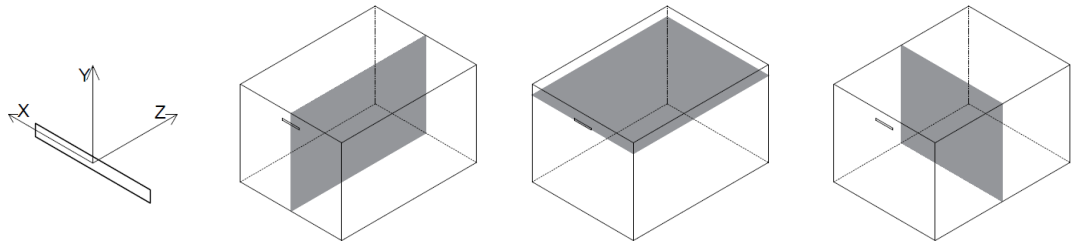

Figure 5. a) X, Y and Z axis b) YZ plane c) XZ plane d) XY plane

The first phase of the test consisted of the comparison of the meshed rendering surface with an opaque one, according to the development of the Coanda effect on each of them. Measurements were made in the same plane with the same airflow to numerically assess the distortion caused by the Coanda effect, considering the dimensional and temperature distortion. A measurement accuracy improvement between 22 and 62 % was obtained, with a mean of 42 % for the meshed rendering surface. Therefore, only the meshed surface was used for the second phase since it was determined that the opaque surface distorts the thermal path.

The second phase consisted of the three-dimensional characterization of the thermal airflow path. IR thermal images were taken every 10 mm, seven at each side of the central axis for each opening. The test was performed by testing three different airflows per opening. The following data were also registered for each IR thermal image: indoor temperature (T_{int}), outdoor temperature (T_{ext}), temperature differential (ΔT), airflow (Q), pressure differential (ΔP), air velocity in the opening inferred through the airflow (V), and the opening dimensions, according to the Continuity Law of Fluids (Table 1).

Table 1. Average data registered during the tests

	A1-Q1	A1-Q2	A1-Q3	A2-Q1	A2-Q2	A2-Q3	A3-Q1	A3-Q2	A3-Q3
Q (m^3/h)	0.53	3.54	6.30	0.53	3.51	6.31	0.52	3.60	6.32
ΔP (Pa)	2.00	-24.39	-97.50	-2.47	-29.41	-90.18	-0.64	-16.50	-58.67
T_{int} (°C)	26.38	26.48	26.48	27.55	27.65	27.64	27.50	27.53	27.52
T_{ext} (°C)	21.57	21.57	21.57	22.70	22.72	22.69	22.61	22.59	22.58
ΔT (°C)	4.80	4.90	4.91	4.86	4.93	4.95	4.90	4.94	4.95
V (m/s)	1.53	10.24	18.23	1.02	6.77	12.17	0.75	5.21	9.14

Each image was firstly processed with Python language to cut, modify the size, and adjust the studied pixels. Secondly, a final image, where each pixel corresponds to the temperature data of every net node, was obtained (Figure 6).

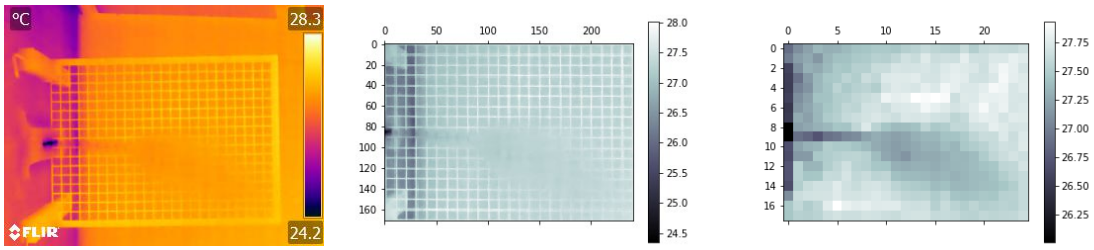

Figure 6. Original thermography b) Discretised thermography c) Thermography of the nodes

The programming language MATLAB was used to simultaneously process all the images. Another column containing the X, Y, and Z coordinates of every node was added to the matrix. Due to the variation of the temperatures in the chamber during the test, a normalization of the temperatures was done using the following equations:

$$\overline{X}_{cut} = \frac{\sum_1^5 (T_{max})}{5} \quad (1)$$

Eq. 1. Temperature averaging, where $\overline{X}_{cut}$ is the average of the five maximum temperatures T_{max} from each of the matrix obtained.

$$T_{m,n} = T_{m0,n0} - \left(T_{max} - \overline{X}_{cut_{min}}\right) \quad (2)$$

Eq. 2. Thermal normalization, where $T_{m,n}$ is the final temperature obtained; $T_{m0,n0}$ is the initial temperature of each value of the matrix; T_{max} is the maximum temperature of each matrix; $\overline{X}_{cut_{min}}$ is the minimum value of each measurement plane $\overline{X}_{cut}$ obtained from Equation 1.

After this normalization, a three-dimensional matrix was composed of the temperature values of every node of the points cloud. This was used to represent the airflow in three dimensions, as well as the calculated measurement planes XY and XZ (Figure 7).

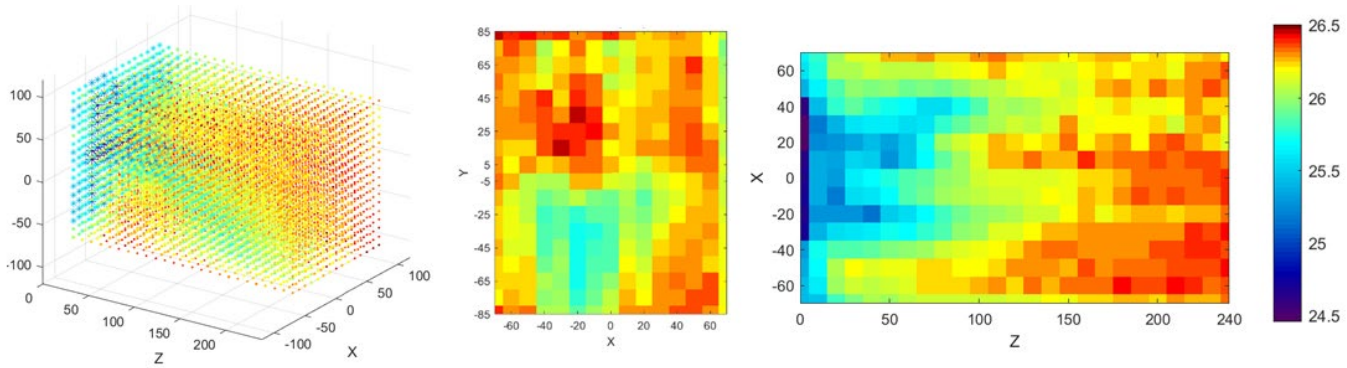

Figure 7. Images of the airflow A3-Q1. a) 3D representation. b) Measurement plane XY at 110 mm from the opening's axis. c) Measurement planes in the XZ axis at -5 mm from the axis.

RESULTS

The following images were obtained from the combination of the openings and airflows as a result of the performance of the twelve tests and the post-processing of the thermal images (Figure 8). It is possible to observe the variation of the airflow path depending on the parameters.

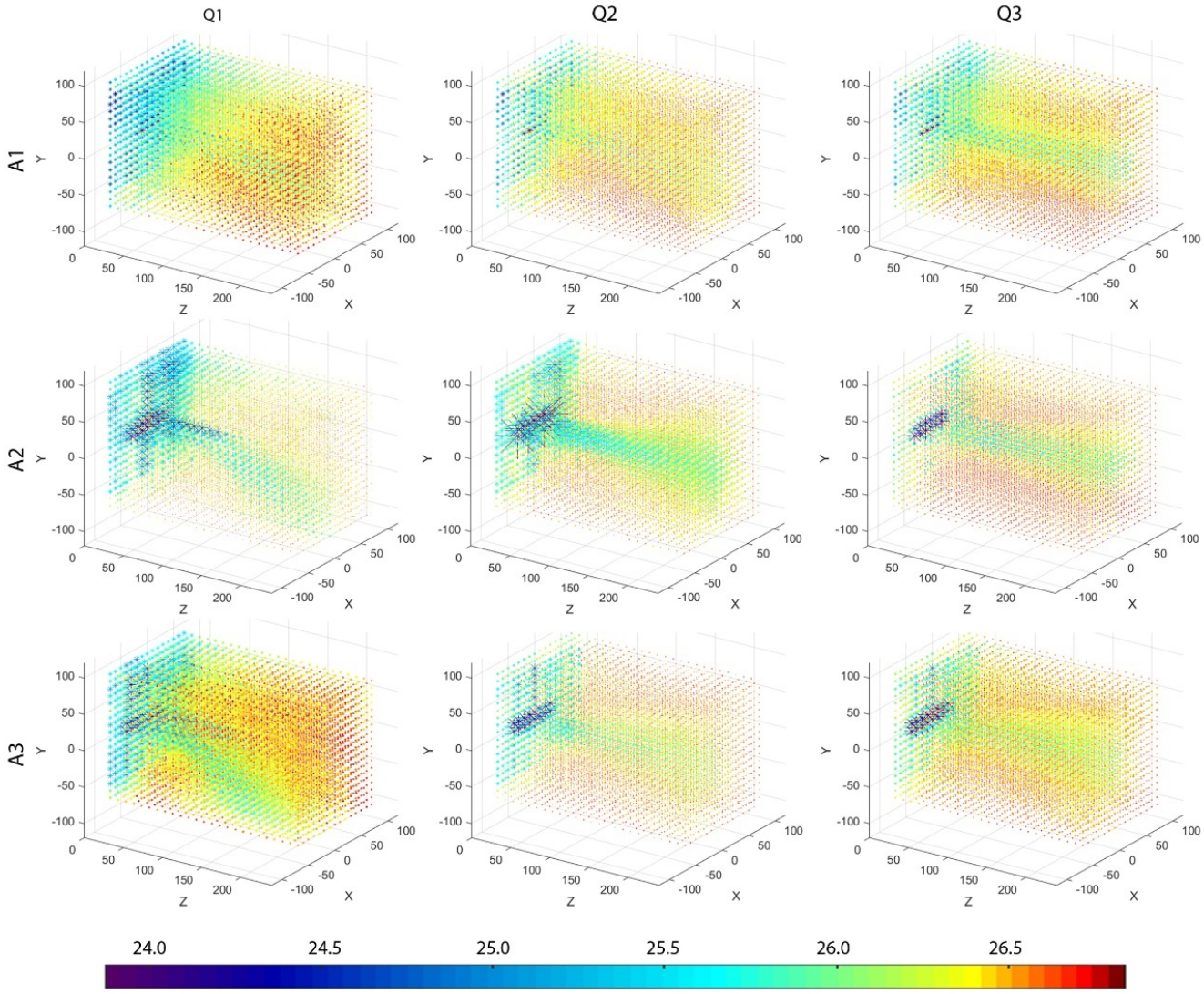

Figure 8. Three-dimensional representation of the airflow. a) A1_Q1 b) A1_Q2 c) A1_Q3 d) A2_Q1 e) A2_Q2 f) A2_Q3 g) A3_Q1 h) A3_Q2 i) A3_Q3

DISCUSSION

The images represent the variation of the thermal airflow path according to the pressure differential and the shape of the opening. It is possible to observe the increment of the cooled Z-axis points of the net due to the variation of the airflow (Figure 8. a, b, c). The drop of the airflow path is visible in the studied zone when the airflow corresponds with Q1 value, while it is not possible to notice it with Q2 and Q3. Regarding the opening shape, it can be observed that the dispersion of the cooled points is greater when the inlet area is bigger.

The calculated images in Figure 9, which correspond with the measurement plane XZ, show that when the distance from the measurement plane to the airflow opening is bigger, the cooled zone is further from the entrance of the airflow due to the descend of the cool air.

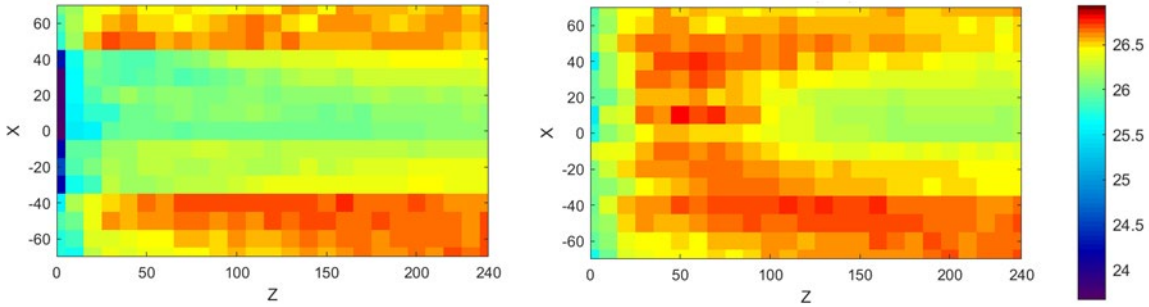

Figure 9. Measurement planes XZ at -5 and -25. A3-Q3 case

In the case of the measurement planes XY obtained from the calculated images (Figure 10), it can be observed that the bigger the distance from the airflow opening to the measurement plane, the greater the cooled zone. However, temperatures are higher due to the dispersion of the air when it enters the room.

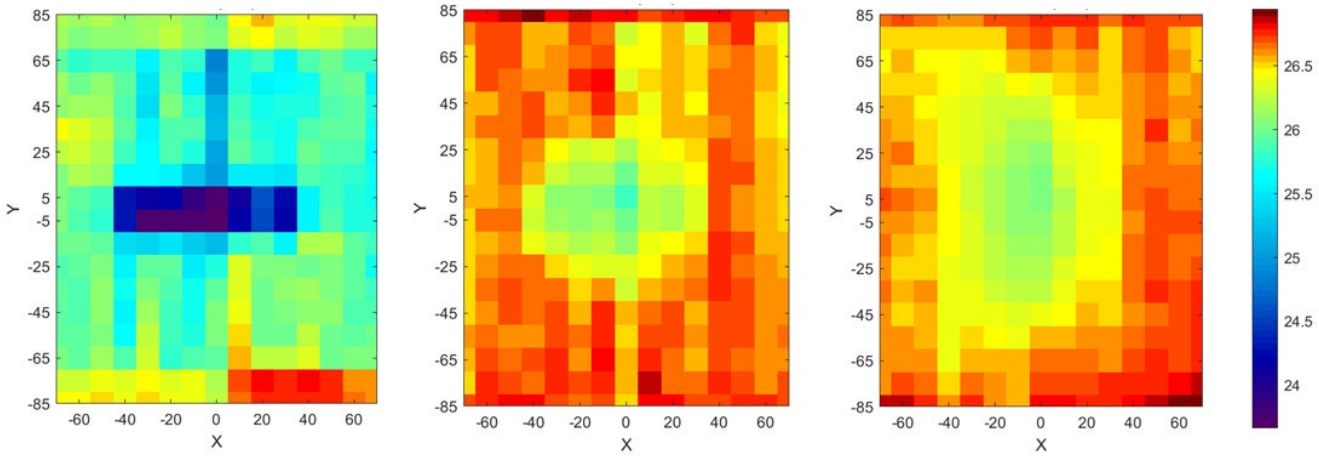

Figure 10. Measurement planes XY at 0, 110, and 240 mm. A3-Q3

CONCLUSION

This study is an approach to represent the shape of the infiltration airflow path using new elements in the process, as the rendering surface and the application of different programming languages for the post-processing of the thermal images. The use of a meshed rendering surface instead of an opaque one meant a 42% reduction in the measuring representation errors due to the avoidance of the Coanda effect. It was demonstrated to be adequate for the determination of the air path through an opening in a controlled environment. The data obtained from thermal images after different post-processing steps result in a good three-dimensional representation of the airflow path.

The methodology described in this paper allows the characterization of the airflow path through an air inlet, which can set the basis for the measurement of component air infiltration in a non-invasive way. Future work could simplify the process due to the reduction of the measurement planes for the representation of the thermal path.

ACKNOWLEDGMENTS

This work has been possible thanks to the funds provided by the Strategy of Entrepreneurship and Youth Employment, Sistema Nacional de Garantía Juvenil, an initiative of the Ministry of Employment and Social Security, Government of Spain, and the European Social Fund of the European Union, the University of Valladolid through the funding of the doctoral program of one of the authors, and the I+D+i National Project INFILES "Energy impact of the airtightness level in residential buildings in Spain: Analysis and characterization of the infiltrations" funded by the Economy and Competitiveness Ministry of the Spanish Government (reference BIA2015-64321-R).

REFERENCES

Barreira, Eva, Ricardo M.S.F. Almeida, and Mariana Moreira. 2017. "An Infrared Thermography Passive Approach to Assess the Effect of Leakage Points in Buildings." *Energy and Buildings* 140: 224–35. http://dx.doi.org/10.1016/j.enbuild.2017.02.009.

Dufour, Marianne Bérubé, Dominique Derome, and Radu Zmeureanu. 2009. "Analysis of Thermograms for the Estimation of Dimensions of Cracks in Building Envelope." *Infrared Physics and Technology* 52(2–3): 70–78. http://dx.doi.org/10.1016/j.infrared.2009.01.004.

Fox, Matthew, David Coley, Steve Goodhew, and Pieter De Wilde. 2015. "Time-Lapse Thermography for Building Defect Detection." *Energy and Buildings* 92: 95–106. http://dx.doi.org/10.1016/j.enbuild.2015.01.021.

Fox, Matthew, Steve Goodhew, and Pieter De Wilde. 2016. "Building Defect Detection: External versus Internal Thermography." *Building and Environment* 105: 317–31. http://dx.doi.org/10.1016/j.buildenv.2016.06.011.

González-Aguilera, D., S. Lagüela, P. Rodríguez-Gonzálvez, and D. Hernández-López. 2013. "Image-Based Thermographic Modeling for Assessing Energy Efficiency of Buildings Façades." *Energy and Buildings* 65: 29–36.

Kirimtat, Ayca, and Ondrej Krejcar. 2018. "A Review of Infrared Thermography for the Investigation of Building Envelopes: Advances and Prospects." *Energy and Buildings* 176: 390–406. https://doi.org/10.1016/j.enbuild.2018.07.052.

Lehmann, B. et al. 2013. "Effects of Individual Climatic Parameters on the Infrared Thermography of Buildings." *Applied Energy* 110: 29–43. http://dx.doi.org/10.1016/j.apenergy.2013.03.066.

Lerma, Carlos, Eva Barreira, and Ricardo M.S.F. Almeida. 2018. "A Discussion Concerning Active Infrared Thermography in the Evaluation of Buildings Air Infiltration." *Energy and Buildings* 168: 56–66. https://doi.org/10.1016/j.enbuild.2018.02.050.

Liu, Wei, Xingwang Zhao, and Qingyan Chen. 2018. "A Novel Method for Measuring Air Infiltration Rate in Buildings." *Energy and Buildings* 168: 309–18.

Royuela-del-Val, Andrés et al. 2019. "Air Infiltration Monitoring Using Thermography and Neural Networks." *Energy and Buildings*.

Sarawade, Akshay A. 2018. "Infrared Thermography and Its Applications : A Review." *2018 3rd International Conference on Communication and Electronics Systems (ICCES)* (Icces): 280–85.